

Seismic experiment and analysis of rectangular bottom strengthened steel-concrete composite columns

Cun Hui^{*1}, Yanzhi Zhu^{1a}, Wanlin Cao^{2b} and Yuanqing Wang^{3c}

¹ School of Architecture and Civil Engineering, Zhongyuan Univeristy of Technology, Zhengzhou, China

² College of Architecture and Civil Engineering, Beijing University of Technology, Beijing, China

³ Department of Civil Engineering, Tsinghua University, Beijing, China

(Received September 11, 2014, Revised September 15, 2015, Accepted November 14, 2015)

Abstract. In order to study the working mechanism of rectangular steel-concrete composite columns subjected to compression-bending load and further determine the seismic performance index, a bottom strengthened rectangular steel reinforced concrete (SRC) column with concealed steel plates and a bottom strengthened rectangular concrete filled steel tube (CFST) columns were proposed. Six column models with different configurations were tested under horizontal low cyclic loading. Based on the experiments, the load-bearing capacity, stiffness and degradation process, ductility, hysteretic energy dissipation capacity, and failure characteristics of the models were analyzed. The load-bearing capacity calculation formulas for a normal section and an oblique section of bottom strengthened rectangular steel-concrete composite columns were presented and a finite element (FE) numerical simulation of the classical specimens was performed. The study shows that the load-bearing capacity, ductility, and seismic energy dissipation capacity of the bottom strengthened rectangular steel-concrete composite columns are significantly improved compared to the conventional rectangular steel-concrete composite columns and the results obtained from the calculation and the FE numerical simulation are in good agreement with those from the experiments. The rectangular steel-concrete composite column with bottom strengthened shows better seismic behavior and higher energy dissipation capacity under suitable constructional requirements and it can be applied to the structure design of high-rise buildings.

Keywords: composite column; steel-concrete; seismic experiment; rectangular section; load-bearing capacity calculation; numerical simulation; finite element

1. Introduction

The steel reinforced concrete (SRC) columns and concrete filled steel tube (CFST) columns, which exhibit high anti-seismic performance, are widely used in high-rise buildings. With the increase of the buildings height, the axial load ratio of composite columns also increases. However, a high axial load ratio can influence the seismic energy dissipation capacity of composite columns. An in-depth study of their seismic performance has important engineering significance. Scholars at

*Corresponding author, Ph.D., E-mail: hui8cun@163.com

^a Professor, E-mail: zhuyanzhi@126.com

^b Professor, E-mail: caowl@bjut.edu.cn

^c Professor, E-mail: wang-yq@mail.tsinghua.edu.cn

home and abroad have done significant research on this topic.

Lu *et al.* (2014) performed experiments of eight SRC columns with high steel ratio and studied on the hysteretic properties of them. Weng *et al.* (2008) studied the properties of SRC columns confined with 5-spirals under seismic cyclic loading. Chen *et al.* (2008) studied the hysteretic behavior of nine SRC columns with high ratio of core steel through experiments. Liao and Han (2010) performed low-cyclic reversed loading tests on square concrete-filled steel tube reinforced concrete columns, studied their hysteretic models, and proposed models of analysis using the nonlinear finite element method. Sav *et al.* (2011) conducted a research about the strong points and weak points of composite columns with high strength concrete and normal strength concrete respectively. Elwan (Elwan and Rashed 2011, Elwan and Omar 2014) studied the behavior of short and slender reinforced concrete columns confined with external GFRP sheets under eccentric loads. Cai and Long (2007) presented an experimental study on the axial load behavior of rectangular concrete-filled steel tubular stub columns with binding bars. Yu *et al.* (2007) presented an experimental study on the behavior of circular, concrete-filled, steel tube stub columns with self-compacting concrete and normal concrete concentrically loaded in compression to failure. Chung *et al.* (2007) provided an efficient method of prediction of the pre- and post-peak hysteretic behavior of concrete-filled square steel tube columns subjected to a combination of constant axial load and cyclic lateral load. Choi *et al.* (2008) proposed the P-M interaction diagram of CFST members with 50 MPa to 110 MPa compressive strength concrete and steel tubes with 262 MPa to 834 MPa yield strength. Zhou *et al.* (2010) studied the seismic behavior of ultra short columns of square tubed high strength reinforced concrete. Hui *et al.* (2012) studied the seismic behavior of bottom strengthened rectangular steel tube reinforced concrete columns.

In this study, a rectangular SRC column and a rectangular bottom strengthened CFST column were proposed and six column models with different configurations were developed under horizontal low cyclic loading. The failure characteristics, load-bearing capacity, stiffness and degradation process, ductility, and hysteretic energy dissipation capacity of the models were analyzed. The load-bearing capacity calculation formula was presented and the finite element numerical simulation was performed.

2. Experimental details

2.1 Specimen design

Six tests on rectangular composite columns were designed. Three rectangular SRC column specimens and three rectangular bottom strengthened CFST columns were tested. The dimensions, steel specifications, and steel bar specifications of the specimens are shown in Fig. 1. All dimensions are in millimeters. The sectional dimension of all the specimens is 280 mm by 400 mm.

The specimen SRCJ-1 is a conventional rectangular SRC column and the sectional dimension of the concealed steel tube is 160 mm by 280 mm. The thickness of the steel tube with higher bending stress is 8 mm and the thickness of the steel tube with lower bending stress is 6 mm. Compared with SRCJ-1, SRCJ-2 is a bottom strengthen specimen and its higher bending stress part at the bottom of steel tube is strengthened with 400-mm high and 8-mm thick steel plates. Compared with SRCJ-2, SRCJ-3 is strengthened with 400-mm high and 6-mm thick steel plates in the other direction.

CFSJ-1 is a conventional rectangular CFST column. The thicknesses of the steel plates perpendicular and parallel to the loading direction are 8 mm and 6 mm, respectively. Compared

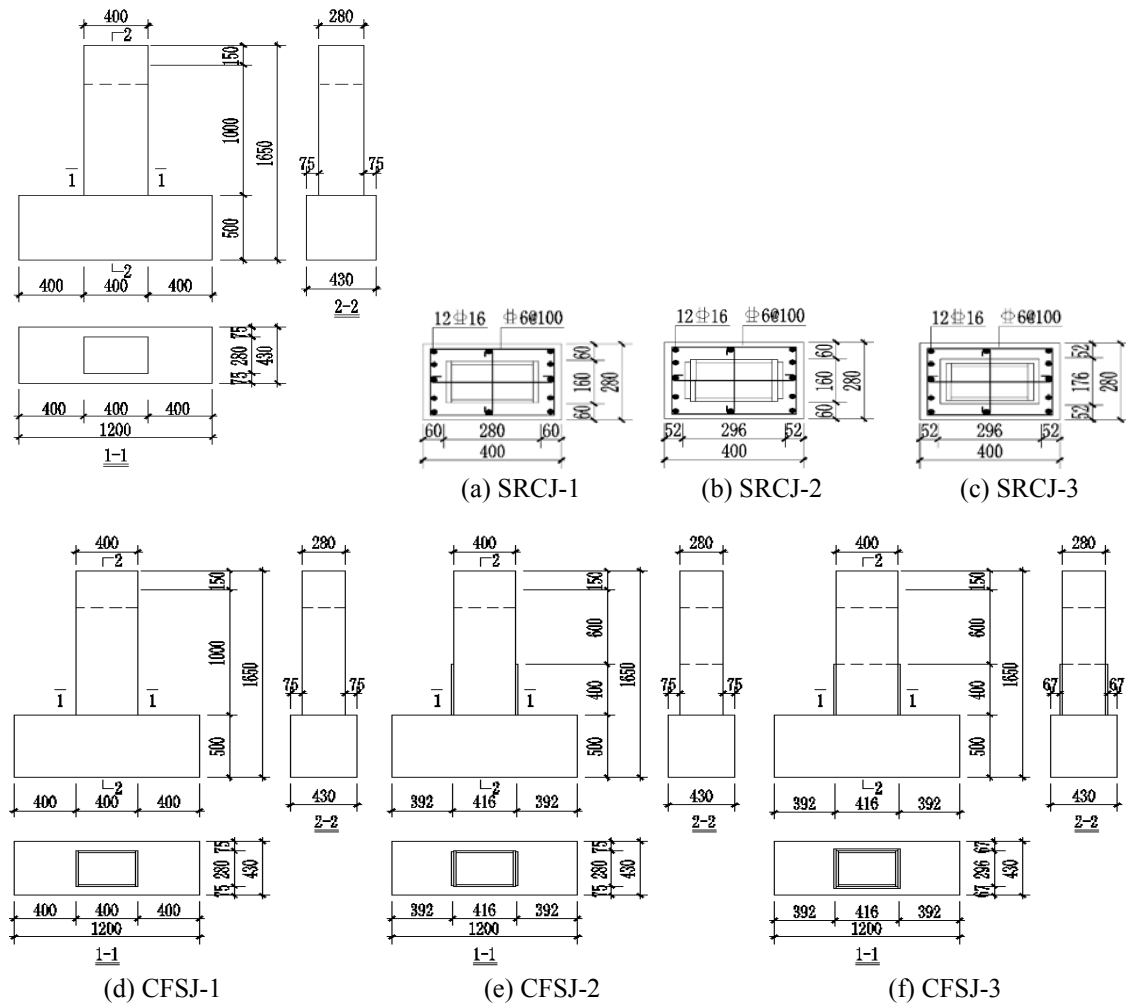


Fig. 1 Steel bars, steel details and geometric dimension of test specimens

Table 1 Measured mechanical properties of steel

Steel plate and steel bar	Yield strength (MPa)	Ultimate strength (MPa)	Elasticity modulus (10^5 MPa)	Elongation rate (%)
$\phi 6$	454	647	2.07×10^5	18.9
$\phi 16$	437	618	1.96×10^5	19.5
6 mm	305	413	2.06×10^5	26.1
8 mm	299	436	2.09×10^5	24.3

with CFSJ-1, CFSJ-2 is a bottom strengthen specimen and its higher bending stress part at the bottom of steel tube is strengthened with 400-mm high and 8-mm thick steel plates. Compared with CFSJ-2, CFSJ-3 is strengthened with 400-mm high and 6-mm thickness steel plates in the other direction.



Fig. 2 Construction procedure of the test specimens

The foundation of the six specimens is composed by rectangular concrete filled steel tubes. The thickness of the steel plates is 8 mm.

The concrete mixes used in the test specimens corresponded to a nominal strength grade C45 from the same batch; its average measured cube concrete compressive strength was 48.72 MPa, and its elasticity modulus was 3.28×10^4 N/mm². For the longitudinal reinforcement and the stirrups in the specimens were used HRB400 steel bars. The mechanical properties of the steel and steel bars used are listed in Table 1.

2.2 Testing procedure

The construction process of the test specimens consists on fabricating the steel bars and plates, numbering the specimens, assembling the reinforcement, and pouring and curing the concrete. Photographs of the construction process are shown in Fig. 2.

The constant vertical loading was applied to the top of the test specimens and the low cyclic loading was applied horizontally to the top of the specimens through a push-pull jack. A constant vertical load of 1730 kN was applied and maintained to the top of the specimens along their vertical axis, while a low cyclic load was applied horizontally to the measured vertical center of

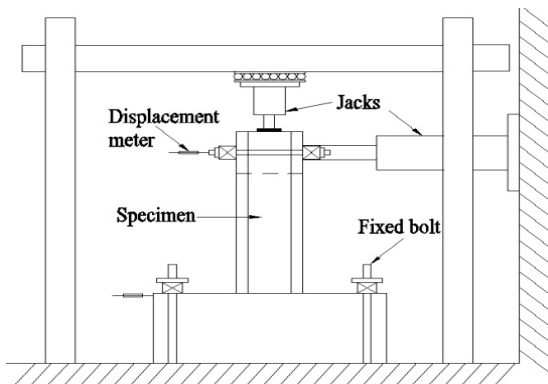


Fig. 3 Schematic view of the test arrangement



Fig. 4 Photograph of the test arrangement

the loading beam (i.e., 1000 mm from the foundation top surface). During loading, a two-step cyclic loading scheme was implemented. A load control program was used prior to the yield load and then a displacement control program was used after the yield point. The test was stopped when the load-bearing capacity dropped to 85 % of the ultimate load. The test arrangement is shown in Figs. 3 and 4.

The force sensors were set at the end of the vertical and horizontal jacks. A displacement transducer was set at the middle of the loading beam along its height. A further displacement transducer was set at the foundation to monitor foundation slippage. Strain measurement points were set at the bottom of the CFST and the middle part of the SP deep beams. Loads, displacements, and strains were recorded by an Integrated Mechanism Program (IMP) data gathering system. The crack development processes, damage, and failure characteristics of the specimens were visually monitored during the tests.

3. Experimental results and analysis

3.1 Load-bearing capacity

Table 2 lists the cracking load, F_c , the effective yielding load, F_y , and the ultimate load-bearing capacity, F_u , of the six specimens, where F_c is the concrete cracking load corresponding to the first occurrence of concrete cracking, and F_u is the ultimate load, which is the maximum horizontal load applied to the specimens. $\mu_{yu} = F_y/F_u$ represents the ratio of the yield load to the ultimate load.

The results from Table 2 show that:

- (1) Compared with SRCJ-1, the cracking load, the yield load, and the ultimate load of SRCJ-2 and SRCJ-3 increase significantly. The cracking load increases by 11.36% and 17.02%, respectively. The yield load increases by 32.54% and 44.18 %, respectively. The ultimate load increases by 29.76% and 36.41 %, respectively.
- (2) The yield load and the ultimate load of CFSJ-2 increase by 19.37% and 18.17% in comparison with CFSJ-1. The yield load and the ultimate load of CFSJ-3 increase by 43.62% and 39.74% in comparison with CFSJ-1.
- (3) The ratio of the yield load to the ultimate load of SRCJ-2 and SRCJ-3 is greater than for SRCJ-1. The ratio of the yield load to the ultimate load of CFSJ-2 and CFSJ-3 is also greater than for CFSJ-1.
- (4) The load-bearing capacity of the specimens with bottom strengthened measures is significantly improved compared to the conventional specimens.

Table 2 Experimental results of yield load and ultimate load

Specimen	F_c /kN	F_y /kN	F_u /kN	F_u (Relative value)	μ_{yu}
SRCJ-1	263.76	477.34	612.21	1.0000	0.780
SRCJ-2	293.71	632.65	794.40	1.2976	0.796
SRCJ-3	308.65	688.24	835.12	1.3641	0.824
CFSJ-1	-	605.30	806.20	1.0000	0.751
CFSJ-2	-	722.57	952.69	1.1817	0.758
CFSJ-3	-	869.12	1126.61	1.3974	0.772

Table 3 Measured displacement and ductility ratio

Specimen	U_c /mm	U_y /mm	U_u /mm	U_d /mm	θ
SRCJ-1	2.76	7.62	18.35	32.05	1/31
SRCJ-2	2.91	8.89	22.94	38.02	1/26
SRCJ-3	2.95	8.99	25.18	51.12	1/20
CFSJ-1	-	11.15	18.48	38.59	1/26
CFSJ-2	-	12.49	25.36	46.66	1/21
CFSJ-3	-	14.95	32.91	52.73	1/19

3.2 Ductility

The measured displacements and ductility ratio of the test specimens are listed in Table 3, where all the displacements were measured at the top loading beams of the composite columns as indicated in Fig. 2. The displacements at various stages shown in Table 3 are defined as: U_c is the cracking displacement, U_y is the yielding displacement, U_u is the ultimate displacement, and U_d is the elastic-plastic ultimate displacement, which is defined as the point at which the load-bearing capacity drops to 85% of the ultimate load. θ is the displacement drift corresponding to U_d and $\mu = U_d/U_y$ is defined as the ductility ratio of the composite column.

The results from Table 3 show that:

- (1) Comparing with the SRCJ-1, the yielding displacement of SRCJ-2 and SRCJ-3 increases by 5.43% and 6.88% respectively, the ultimate displacement of SRCJ-2 and SRCJ-3 increases by 12.34% and 17.98% respectively, the elastic-plastic ultimate displacement of SRCJ-2 and SRCJ-3 increases by 18.63% and 59.50% respectively, and the ductility ratio of SRCJ-2 and SRCJ-3 increases by 1.69% and 35.19% respectively. The results show that the ductile behavior and the elastic-plastic deformation ability of SRCJ-2 and SRCJ-3 highly exceed the values for the conventional SRC column SRCJ-1.
- (2) Comparing with the CFSJ-1, the yielding displacement, the ultimate displacement, and the elastic-plastic ultimate displacement of CFSJ-2 increases by 12.02%, 37.23%, and 20.91%, respectively. Comparing with the CFSJ-1, the yielding displacement, the ultimate displacement, and the elastic-plastic ultimate displacement of CFSJ-3 increases by 43.05%, 78.08%, and 36.64%, respectively. Comparing with the CFSJ-2, the yielding displacement, the ultimate displacement, and the elastic-plastic ultimate displacement of CFSJ-3 increases by 19.70%, 29.77%, and 13.01%, respectively. These results show that the elastic-plastic deformation capacity of the bottom strengthened rectangular CFST column is better than for a traditional column.
- (3) The ductility ratio of CFSJ-2 increases by 7.95% in comparison with the ductility ratio of CFSJ-1. During the experiment, the elastic-plastic ultimate displacement was not reached when the load-bearing capacity was reduced to 85% ultimate load. Therefore, the actual ductility ratio must be greater than the value presented in Table 3.
- (4) The displacement drift corresponding to the ultimate load of CFSJ-2 and CFSJ-3 is 1/39 and 1/30 respectively, which corresponds to a rating of “no collapse under serious earthquakes” per the Chinese Code GB50011 (2010). The demands of the code is no damage in minor earthquakes, mendable in moderate earthquakes and no collapsing with

Table 4 Measured stiffness and stiffness degradation coefficient

Specimen	$K_0/\text{kN}\cdot\text{mm}^{-1}$	$K_c/\text{kN}\cdot\text{mm}^{-1}$	$K_y/\text{kN}\cdot\text{mm}^{-1}$	K_y (Relative value)	β_{y_0}	β_{y_0} (Relative value)
SRCJ-1	145.63	95.57	54.29	1.0000	0.372	1.0000
SRCJ-2	161.98	100.93	57.85	1.0656	0.357	0.9597
SRCJ-3	175.58	104.63	61.14	1.1262	0.348	0.9355
CFSJ-1	172.13	-	62.64	1.0000	0.364	1.0000
CFSJ-2	184.23	-	71.16	1.1360	0.386	1.0604
CFSJ-3	192.16	-	76.56	1.2222	0.398	1.0934

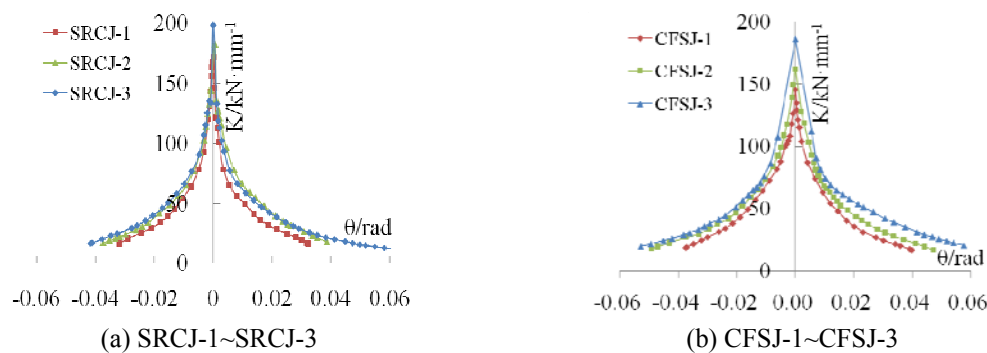


Fig. 5 “K-θ” stiffness degradation curves

serious earthquakes. The code GB50011 defines the maximum displacement drift is 1/50 under serious earthquakes. This shows that these specimens exhibit an increased ability of anti collapse. The SRCJ-2 and the SRCJ-3 display the same performance.

3.3 Stiffness

The measured stiffness and stiffness degradation coefficients of the test specimens are listed in Table 4, where K_0 is the initial tangent stiffness, K_c is the secant stiffness corresponding to the state of the column at initial cracking, and K_y is the secant stiffness corresponding to the yield state of the column. $\beta_{y_0} = K_y/K_0$ is the stiffness degradation coefficient, which is the ratio of the stiffness from the yielding state to the initial elastic state.

Stiffness attenuation curves of three rectangular SRC columns with concealed double steel plates are shown in Fig. 5(a) and stiffness attenuation curves of three bottom strengthened rectangular CFST columns are shown in Fig. 5(b).

The results from Table 4 and Fig. 5 show that:

- (1) The stiffness degradation of the specimens can be divided into three different phases, which corresponds to fast degradation, sub-fast degradation, and slow degradation along with the progress of the composite columns from fine cracking, cracking, and yielding to elastic-plastic maximum displacement.
- (2) Comparing with SRCJ-1, the initial stiffness of SRCJ-2 and SRCJ-3 increases by 7.03% and 11.64% respectively and the yield stiffness of SRCJ-2 and SRCJ-3 increases by 13.60% and 22.22% respectively. The three specimens follow a similar stiffness degradation rule.

This shows that the initial stiffness and yield stiffness of the bottom strengthen columns increase significantly.

- (3) Comparing with CFSJ-1, the initial stiffness of CFSJ-2 and CFSJ-3 increases by 11.23% and 20.57% respectively and the yield stiffness of CFSJ-2 and CFSJ-3 increases by 6.56% and 12.62%, respectively. The stiffness degradation coefficient of CFSJ-1, CFSJ-2, and CFSJ-3 are close to each other.

3.4 Hysteretic behavior and energy dissipation capacity

The hysteretic behavior of the test specimens can be analyzed by the shape of the hysteretic loops. The measured load-displacement hysteretic loops of the specimens are shown in Fig. 6. The measured skeleton curves of the models are shown in Fig. 7. It can be observed that:

- (1) The hysteresis loops of SRCJ-1 are very plump and rounder than SRCJ-2 and SRCJ-3. The hysteresis loops of SRCJ-2 are rounder and less pinched in the middle than the loops of SRCJ-3. The hysteresis loops of SRCJ-1 are clearly rounder and exhibit less pinching when compared to the loops of SRCJ-2 and more rounder when compared to the loops of SRCJ-3, but the load-bearing capacity of SRCJ-3 is the highest of the three test specimens. The hysteresis loops of SRCJ-3 reflect the bending and shear deformation character. Therefore, out of the three test specimens, SRCJ-3 exhibits the highest energy dissipation capacity.
- (2) The hysteresis loops of CFSJ-1 are very plump and rounder than the loops of CFSJ-2 and CFSJ-3. This reflects that the main deformation behavior of CFSJ-1 is bending. The pinching of the loops of CFSJ-3 are the most severe observed between the loops of CFSJ-1, CFSJ-2, and CFSJ-3. However, the inner area of the hysteretic loops of CFSJ-3 is the largest.

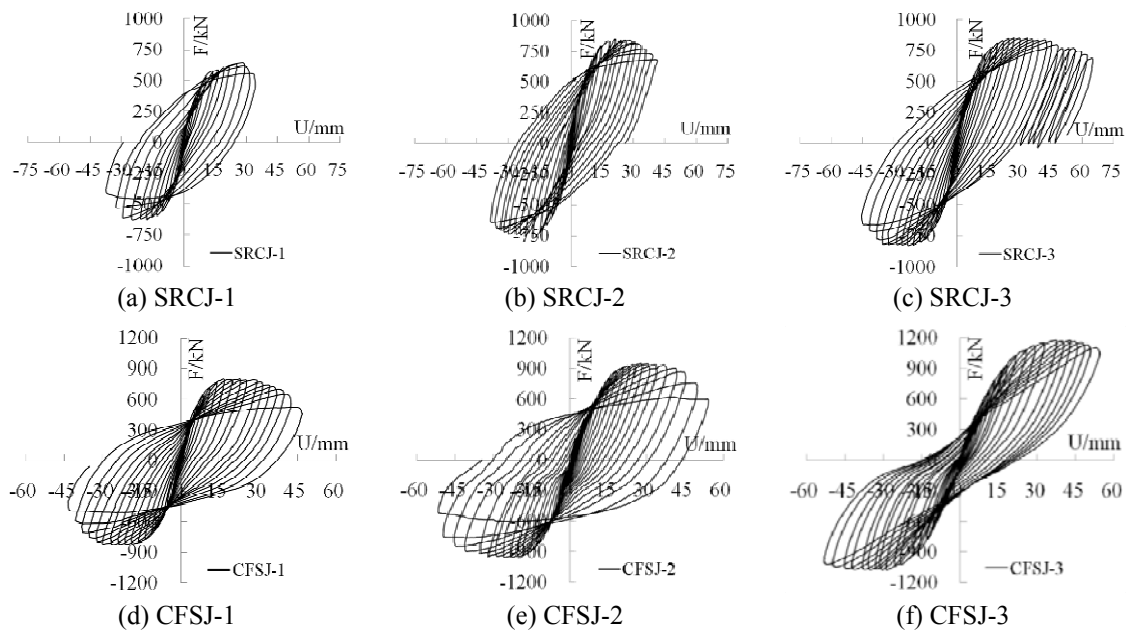


Fig. 6 “Load-displacement” hysteretic curves of test specimens

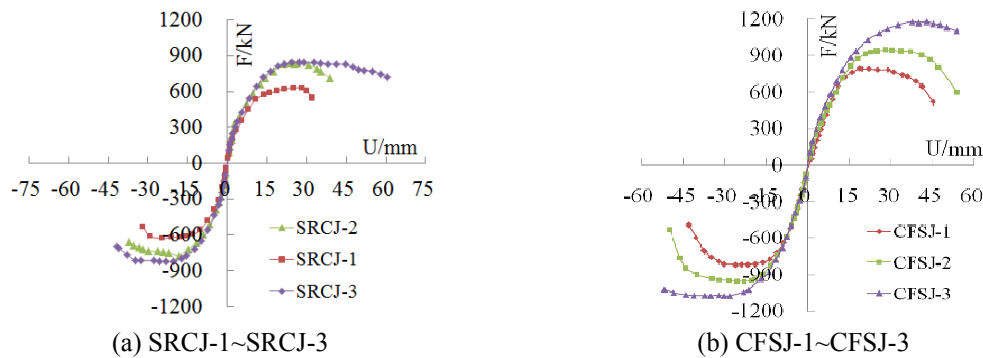


Fig. 7 Skeleton curves of test specimens

Table 5 Measured results of energy dissipation

Specimen	$E_p/\text{kN}\cdot\text{mm}$	E_p (Relative value)
SRCJ-1	42510	1.0000
SRCJ-2	57085	1.3429
SRCJ-3	82591	1.9428
CFSJ-1	44419	1.0000
CFSJ-2	62971	1.4177
CFSJ-3	83623	1.8826

The energy dissipation capacity of the test specimens was evaluated by calculating the inner area of the hysteretic loops and using this as an index. The measured values of energy dissipation capacity (E_p) are listed in Table 5. It can be observed that: The measured energy dissipation capacity values of SRCJ-2 and SRCJ-3 are higher by 34.29% and 94.28%, respectively, over values of SRCJ-1. The measured energy dissipation capacity values of CFSJ-2 and CFSJ-3 are higher by 41.77% and 88.26%, respectively, over the values of CFSJ-1. This demonstrates that the energy dissipation capacities of the strengthened SRC columns and bottom strengthened CFST columns are significantly higher than for traditional columns.

3.5 Failure patterns

Photographs of the test specimens at failure mode are shown in Fig. 8. Through strengthening the bottom area of rectangular composite columns, the flexural and shear capacity of energy dissipation of the steel plates can be significantly improved. The damage processes of specimens verify that the structural measures are effective. The processes of cracking and failure are described as follows:

- (1) The concrete crack in the traditional SRC column SRCJ-1 appears on the outside of the long side of the cross section, on the bottom zone first, then the cracks appear on the short side of the cross section, on the tensile zone. With the increase of the horizontal displacement, the crack on the long side of the cross section extends forming X-shape cross diagonal cracks that increase from the bottom to upper zone. Then, the crack width increases quickly and the steel bars and plates yield. The main bars on the corner are

exposed and bent, meanwhile, the concrete at the corner of the bottom zone is crushed and shed. At this point, the specimen loses its load-bearing capacity. The bottom area of the column is severely damaged and the upper becomes lighter. After the experiment, the concrete of the bottom zone is removed and it is observed that the steel tube is convex except at the part where is connected to the steel bars. This shows that the steel bars improve the restraint effect of the steel tube.

- (2) The failure mode of the composite column SRCJ-2 is almost identical to SRCJ-1 at the beginning. With the increase of the horizontal displacement, cracks on the tensile zone of the cross section increase and mainly appear at a height of 500 mm from the bottom zone. The vertical cracks appear at the location of the longitudinal bars on the long side of the cross section. The concrete protective layer of longitudinal bars is crushed and shed leaving the stirrups exposed. At this point, the specimen loses its load-bearing capacity. The difference between SRCJ-2 and SRCJ-1 is that in column SRCJ-2, the cracks widely distribute over the web. The shear capacity of the web along the entire height is almost fully developed.
- (3) The failure process of the composite column SRCJ-3 is almost identical to SRCJ-2. With the increase of the horizontal displacement, horizontal cracks on the short side and oblique cracks on the long side of the cross section increase and extend. The cracks appear on the 400-mm high plastic hinge zone of the bottom part. At last, the protective concrete layer of the corner longitudinal bars is crushed and shed, leaving the longitudinal steel bars and the stirrups exposed. At this point, the specimen loses its load-bearing capacity.
- (4) There is no obvious damage phenomenon on the CFSJ-1 before the column yields. With the increase of the horizontal displacement, one bulge appears on the outside of the compressive short side of the cross section located 70 mm from the top surface of the foundation. Then, the bulges appear on the outside of the compressive long side of the cross section, and lastly, the bulges appear on the entire cross section. The fillet weld of the steel tube cracks and the concrete in the steel tube crushes and sheds. The plastic hinge domain concentrates on the bottom of the column within 250 mm of height. Above of the plastic hinge domain, the damage of cross section is lighter. The shear capacity of the steel plate along the entire height is not fully developed.
- (5) The failure mode of the composite column CFSJ-2 is almost identical to CFSJ-1 at the beginning. With the increase of the horizontal displacement, one bulge appears on the outside of the strengthened steel plates. The distance between the center of the bulge and the bottom of the column is 80 mm. The bulge of the strengthened steel plates can restrain the inner steel tube. There are X-shaped cross diagonal bulges on the long side of the cross section at the bottom strengthened region. The fillet weld at the corner part of steel tube at the bottom zone cracks first, then the concrete in the steel tube crushes and sheds, and the load-bearing capacity decreases. The plastic hinge domain concentrates at the bottom of the column within 200 mm of height. The shear yielding bulges on the bottom strengthened region are lighter than CFSJ-1 and that can improve bending resistance of the bottom region. Above of the plastic hinge domain, the damage of cross section is lighter. The shear capacity of the web steel plate along the entire height is almost fully developed.
- (6) The failure process of the composite column CFSJ-3 is almost identical to CFSJ-2. The bulge appears first on the outside of the short side of the strengthened steel plates. The distance between the center of the bulge and the bottom of the column is 90 mm. With the increase of the horizontal displacement, the bulge appears on the short side of the cross

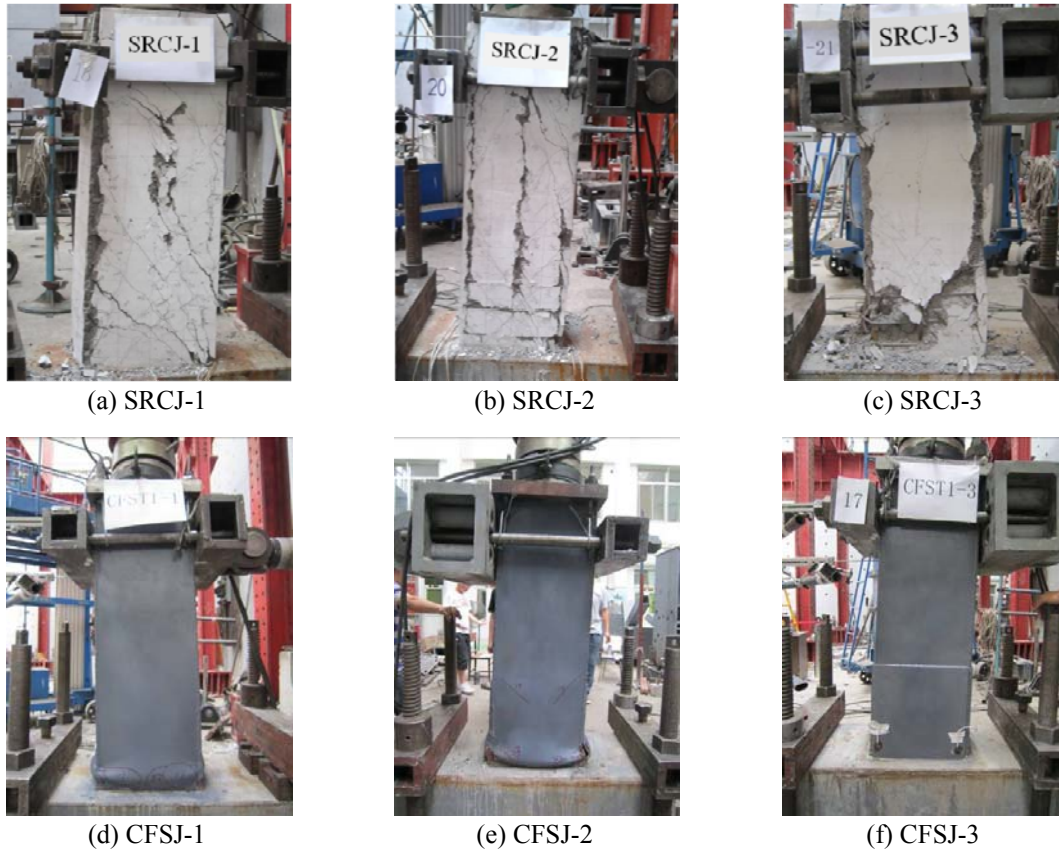


Fig. 8 Failure modes of test specimens

section of the no strengthened zone, and the distance between the bulge and the bottom of the column is 470 mm. The bending resistance of the cross section is significantly improved and the shear resistance of the cross section is moderately improved, with its surrounding part at the bottom of steel tube welded with steel plates. Therefore, the load-bearing capacity is significantly improved while the shear yielding bulge at the bottom is not notorious. The bending and shear resistance ability reach a reasonable match. The shear and bending capacity along the entire height is fully developed.

4. Calculating the load-bearing capacity

4.1 SRC columns

4.1.1 Bending bearing capacity of a normal section

This experimental study shows that the failure of composite columns mainly exhibit bent broken characteristics. Therefore, the following basic assumptions were made:

- (1) Bernouli's principle holds for reinforced concrete members at the ultimate state; this principle simply states that a plane section remains plane.

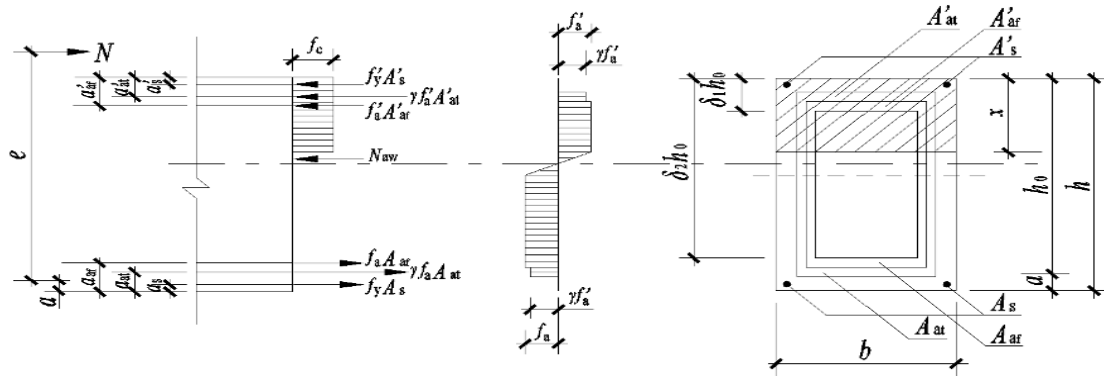


Fig. 9 Mechanical model of the load-bearing capacity of SRC columns

- (2) Any tensile strength in the concrete below the neutral axis was considered insignificant.
- (3) The stress-strain relationship of concrete in compression is evaluated by the current Chinese code GB50010 (2010).
- (4) The strain at the external fiber of the compression zone reaches a value of 0.0033.
- (5) Steel in the experimental structures exhibited elastic behavior before yielding and maintained a yielding stress after the yield point.

The bottom cross sections of rectangular SRC columns are bent yielding. The mechanical model of the load-bearing capacity is shown in Fig. 9.

Here, f_y and f'_y are the tensile and compressive yield strengths of the steel bars, respectively. f_a and f'_a are the tensile and compressive yield strengths of the steel plates, respectively. f_c is the compressive strength of concrete. A_s and A'_s are the sectional areas of the steel bars in the tension and compression zones, respectively. A_{af} and A'_{af} are the tensile and compressive sectional areas of the concealed steel tube, respectively. A_{at} and A'_{at} represent the sectional areas of the outer strengthened steel plate in the tension and compression zones, respectively. a_s and a'_s are the distances from the points of resultant forces of the tensile and compressive steel bars, respectively, to the near external fiber of the section. a_{af} and a'_{af} are the distances from the points of resultant forces of the tensile and compressive steel plates, respectively, to the near external fiber of the section. a_{at} and a'_{at} are the distances from the points of resultant forces of the tensile and compressive strengthened steel plates, respectively, to the near external fiber of the section. a represents the distance from the points of resultant forces of the tensile steel bars and steel plates to the near external fiber of the section. x is the depth of the compression zone. β_1 is the characteristic value of the equivalent rectangular stress diagram, $\beta_1 = 0.8$. h_0 represents the effective height of the cross section. h is the height of the cross section. b is the width of the cross section. N , V , and M represent the sectional axial force, shearing force, and bending moment of the column, respectively. $e_0 = M/N$ is the initial eccentricity of the axial force with respect to the centroid of section.

According to the equilibrium equation

$$N = f_c b x + f'_y A'_s + f'_a A'_{af} - f_y A_s - f_a A_{af} + N_{aw} \quad (1)$$

$$Ne = f_c b x (h_0 - x/2) + f'_y A'_s (h_0 - a'_s) + f'_a A'_{af} (h_0 - a'_a) + M_{aw} \quad (2)$$

where

$$N_{aw} = [2.5x/h_0 - (\delta_1 + \delta_2)] t_w h_0 f_a \quad (3)$$

$$M_{aw} = [0.5(\delta_1^2 + \delta_2^2) - (\delta_1 + \delta_2) + 2.5x/h_0 - (1.25x/h_0)^2] t_w h_0^2 f_a \quad (4)$$

δ_1 and δ_2 are the ratios of the distances between top and bottom of the steel plates in the web, respectively to the upper edge of the cross section to h_0 . t_w is the height of the entire steel plate in the long side of the cross section.

The horizontal load-bearing capacity of the composite column is

$$F = M / H \quad (5)$$

where, H is the distance from the horizontal loading point to the top surface of the foundation.

γ is the reduction factor of the strengthened steel plate to horizontal load-bearing capacity, $\gamma = 0.85$. It considers the influence on the wholeness of the strengthened steel plate and the initial steel plates.

4.1.2 Shear bearing capacity of an oblique section

Based on the standard “technical specification for steel reinforced concrete composite structure” (2001), the equation for shear bearing capacity of an oblique section is the following

$$V = \frac{0.2}{\lambda + 1.5} f_c b h_0 + f_{yv} \frac{A_{sv}}{s} h_0 + \frac{0.58}{\lambda} f_a t_w h_w + 0.07 N \quad (6)$$

Here, λ is the shear span ratio. f_{yv} is the tensile yield strength of the stirrups. A_{sv} is the total sectional areas of the stirrups in the same cross section. s is the distance between each two stirrups. h_w is the height of the concealed steel tube. If $N > 0.3f_c A_c$, it should be made $N = 0.3f_c A_c$.

4.2 CFST columns

4.2.1 Bending bearing capacity of a normal section

The bottom cross sections of rectangular CFST columns are bent yielding. The mechanical model of the load-bearing capacity is shown in Fig. 10. Fig. 10(a) shows the force schematic diagram of the cross section, Fig. 10(b) shows the stress distribution diagram of the concrete, Fig. 10(c) shows the stress distribution diagram of the steel plate, and Fig. 10(d) shows the dimension details.

Here, N_{al} and N'_{al} are the tensile and compressive load of the short side of the steel tube, respectively, $N_{al} = b t_h f_a$, $N'_{al} = 2 b t_h f_a$. N_{a2} and N'_{a2} are the tensile and compressive load of the long side of the steel tube, respectively, $N_{a2} = 2 t_b (h_c - x) f_a$, $N'_{a2} = 2 t_b x f_a$. N_c is the compressive load of the concrete, $N_c = b_c x f_c$. h_c and b_c are the height and width of the concrete cross section, respectively. t_h and t_b are the entire width of the short side and long side steel plates, respectively, $t_h = t_{h1} + t_{h2}$, $t_b = t_{b1} + t_{b2}$. t_{h1} and t_{b1} are the width of the inner short side and long side steel plates, respectively. t_{h2} and t_{b2} are the width of the strengthened short side and long side steel plates, respectively.

Based on the standard “Technical Specification for Structures with Concrete-filled Rectangular Steel Tube Members” (2004), the equation for bending bearing capacity of a normal section is the following

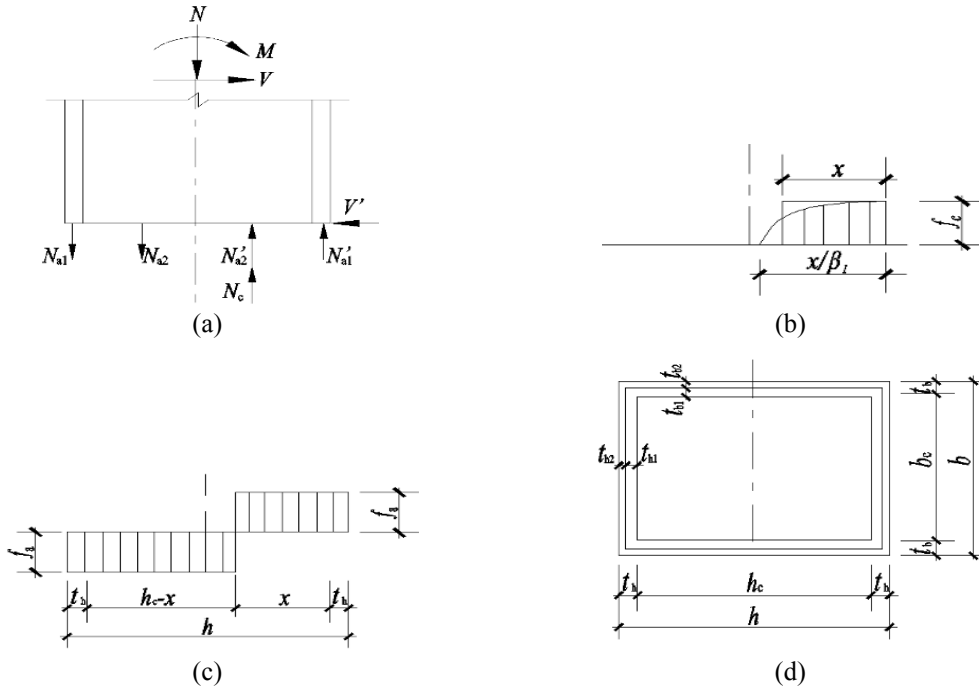


Fig. 10 Mechanical model of capacity of test specimen with significant eccentricity load

$$\frac{N}{N_u} + (1 - \alpha_c) \frac{M}{M_u} = 1 \tag{7}$$

where, N_u is the compressive load-bearing capacity under axial compression, $N_u = f_a A_a + f_c A_c$. M_u is the bending bearing capacity under simple bending load, $M_u = [t_h^2 b + t_h b h_c + t_b (h_c - x) h_c] f_a$, $x = \frac{2h_c t_b}{b_c f_c / f_a + 4t_b}$, $\alpha_c = f_c A_c / (f_a A_a + f_c A_c)$.

The horizontal load-carrying capacity of the CFST columns refers to Eq. (3).

According the Eqs. (1) to (5), the moment-load (M-N) charts of SRC columns and CFST can be obtained, which are shown in Fig. 11.

4.2.2 Shear bearing capacity of an oblique section

Based on the standard “Technical Specification for Steel Reinforced Concrete Composite Structure” (2001), the equation for shear bearing capacity of an oblique section is

$$V = \frac{2}{\lambda + 1.5} f_t b_c h_c + \frac{0.58}{\lambda} f_a t_b h + 0.07N \tag{8}$$

where, λ is the shear span ratio. If $N > 0.3f_c A_c$, it should be made $N = 0.3f_c A_c$.

4.3 Calculation results

The test strengths of the concrete, steel bar, and steel plate in the models are used in the

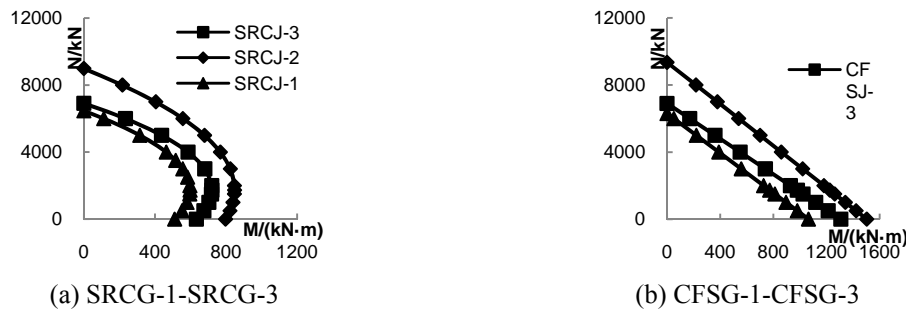


Fig. 11 M-N curves of the models

equations described above. The calculated values and test results of the ultimate horizontal load-bearing capacity and shear bearing capacity of the oblique section are shown in Table 6. Table 6 demonstrates a good agreement between the equations and the test results. The simplified formulas presented above can be used to design specific examples of these composite columns and predict their load-bearing capacities.

5. Elastic-plastic finite element numerical simulations

5.1 Finite element model

The “Damaged Plasticity” model provided by the ABAQUS software and the concrete stress-strain ($\sigma-\varepsilon$) relationship from Han (2004) were adopted for modeling the concrete. The cube compressive strength and elastic modulus of concrete are determined using the material properties and results from the tests and will be used in the Finite Element Model (FEM) analysis. The Poisson’s ratio of concrete is 0.2. The “ $\sigma-\varepsilon$ ” equation for compressive concrete is given as follows

$$y = \begin{cases} 2x - x^2 & x \leq 1 \\ \frac{x}{\beta(x-1)^{\eta} + x} & x > 1 \end{cases} \quad (9)$$

Table 6 Calculated and experimental results of load-bearing capacity

Specimen	Shear bearing capacity of an oblique section		Load-bearing capacity of a normal section			
	Upper zone (kN)	Bottom strengthened zone (kN)	Calculated value of upper zone (kN)	Calculated value of bottom strengthened zone (kN)	Test value (kN)	Relative error (%)
SRCJ-1	887.91	887.91	597.89	597.89	612.21	2.34
SRCJ-2	887.91	898.67	597.89	733.26	794.40	7.69
SRCJ-3	887.91	1327.23	597.89	863.81	835.12	-3.44
CFSJ-1	1210.94	1210.94	740.61	740.61	806.20	8.14
CFSJ-2	1210.94	1265.87	740.61	935.13	952.69	1.84
CFSJ-3	1210.94	2155.08	740.61	1166.97	1126.61	-3.58

where, $x = \varepsilon / \varepsilon_0$; $y = \sigma / \sigma_0$; $\varepsilon_0 = \varepsilon_c + [1330 + 760(f_c/24 - 1)]\varepsilon^{0.2}$; $\varepsilon = \frac{f_y A_s}{f_c A_c}$; $\varepsilon_{cc} = 1300 + 12.5f_c$; $\eta = 1.6 + 1.5/x$; when $\zeta \leq 3$, $\beta = \frac{f_c}{1.35\sqrt{1+\zeta}}$, when $\zeta > 3$, $\beta = \frac{f_c^{0.1}}{1.35\sqrt{1+\zeta}(\zeta-2)}$; A_s and A_c are the area of the steel plates and the concrete, respectively.

The “ σ - ε ” equation for tensile concrete is given as follows

$$\sigma = \begin{cases} \sigma_p [1.2(\frac{\varepsilon}{\varepsilon_p}) - 0.2(\frac{\varepsilon}{\varepsilon_p})^6] & \varepsilon \leq \varepsilon_p \\ \sigma_p (\frac{\varepsilon}{\varepsilon_p}) \frac{1}{0.31\sigma_p^2 (\frac{\varepsilon}{\varepsilon_p} - 1)^{1.7} + \frac{\varepsilon}{\varepsilon_p}} & \varepsilon > \varepsilon_p \end{cases} \quad (10)$$

where, $\sigma_p = 0.26(1.5f_{ck})^{2/3}$ is the peak tensile stress and $\varepsilon_p = 43.1\sigma_p(\mu\varepsilon)$ is the strain corresponding to the peak tensile stress.

For steel plates and steel bars, the “Plasticity” model from the ABAQUS software was adopted and an elastic strengthened tri-linear curve was adopted for the stress-strain relationship. The stress-strain relationship after yielding was simplified as a skewed line. The equation for “ σ - ε ” of tensile concrete is given as follows

$$\sigma_s = \begin{cases} E_s \varepsilon_s & 0 \leq \varepsilon_s < \varepsilon_y \\ f_y & \varepsilon_y \leq \varepsilon_s < \varepsilon_h \\ f_y + (\varepsilon_s - \varepsilon_h)E_p & \varepsilon_s \geq \varepsilon_h \end{cases} \quad (11)$$

where, E_s is the elasticity modulus of the steel. $E_p = 0.01E_s$, $\varepsilon_y = f_y / E_s$, $\varepsilon_h = 10f_y / E_s$.

The solid element C3D8R from the ABAQUS elements library, was used for core concrete, common concrete, and steel tube, while the truss element T3D2 was used for steel bars.

The interface model between the steel tube and the core concrete composed of contact in the lateral axis and stick-slip along the tangential axis. The “Hard Contact” model was adopted for the contact on the lateral axis and the “Coulomb Friction” model was adopted for the stick-slip along the tangential axis. The coefficient of friction between the steel tube and the core concrete was set as 0.3. The steel bars and concealed steel plates were embedded in concrete. The bottom of the CFST columns and the shear wall were all rigidly fixed. A vertically distributed load was applied to the top of the loading beam and a horizontal displacement was applied to the end of the loading beam.

5.2 Results and analysis

5.2.1 Load-bearing capacity

A numerical simulation was performed for the six test specimens using the method described above. Fig. 12 compares the simulated and actual test backbone curves. The simulation results are in good agreement with the test results.

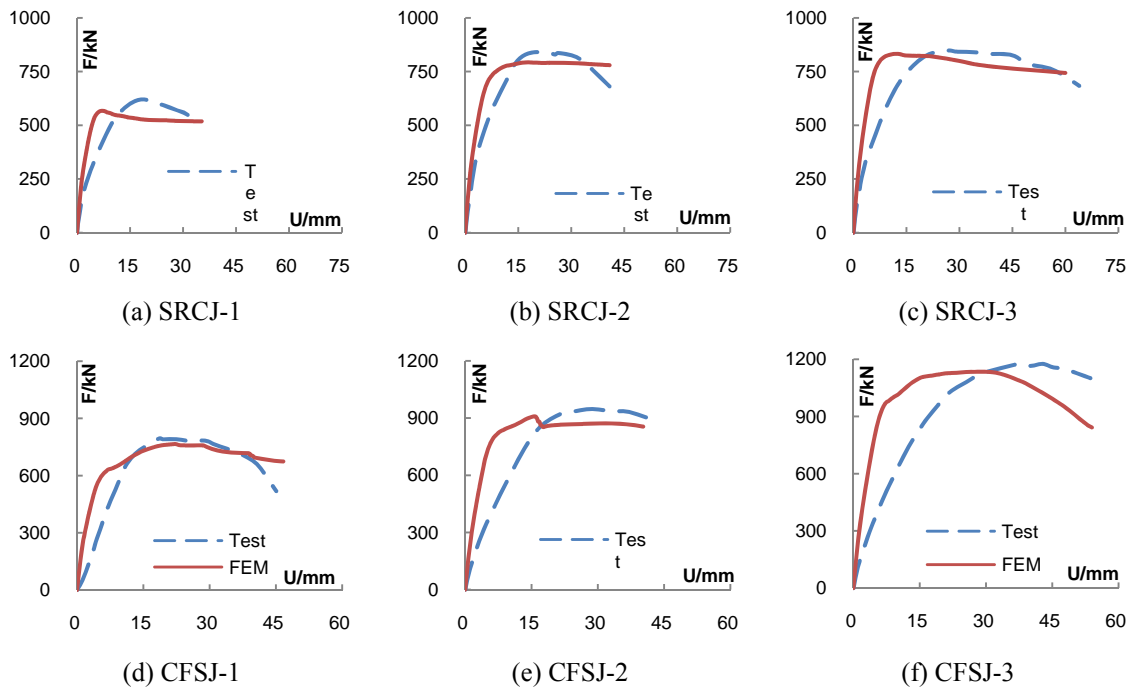


Fig. 12 Compared skeleton curves between calculated and test results of specimens

where, E_s is the elasticity modulus of the steel. $E_p = 0.01E_s$, $\varepsilon_v = f_v / E_s$, $\varepsilon_h = 10f_v / E_s$.

The solid element C3D8R from the ABAQUS elements library, was used for core concrete, common concrete, and steel tube, while the truss element T3D2 was used for steel bars.

The interface model between the steel tube and the core concrete composed of contact in the lateral axis and stick-slip along the tangential axis. The "Hard Contact" model was adopted for the contact on the lateral axis and the "Coulomb Friction" model was adopted for the stick-slip along the tangential axis. The coefficient of friction between the steel tube and the core concrete was set as 0.3. The steel bars and concealed steel plates were embedded in concrete. The bottom of the CFST columns and the shear wall were all rigidly fixed. A vertically distributed load was applied to the top of the loading beam and a horizontal displacement was applied to the end of the loading beam.

5.2 Results and analysis

5.2.1 Load-bearing capacity

A numerical simulation was performed for the six test specimens using the method described above. Fig. 12 compares the simulated and actual test backbone curves. The simulation results are in good agreement with the test results.

5.2.2 Mechanical characteristics of the different stages of deformation

To study the mechanical characteristics of the different stages of the test specimens, the typical specimens SRCJ-3 and CFSJ-3 were selected to be analyzed. The mechanical states of yielding condition, peak condition, and damage condition are studied.

Table 7 Calculated and experimental results of ultimate load bearing capacity

Specimen	Calculated value (kN)	Test value (kN)	Relative error (%)
SRCJ-1	567.52	612.21	7.30
SRCJ-2	792.95	794.40	0.18
SRCJ-3	832.84	835.12	0.27
CFSJ-1	765.57	806.20	5.04
CFSJ-2	908.74	952.69	4.61
CFSJ-3	1134.25	1126.61	0.68

5.2.2.1 SRCJ-3

The stress diagrams of steel bars, concealed steel plates, and strengthened steel plates of SRCJ-3 at yielding condition are shown in Fig. 13. All stresses are expressed in MPa. It can be observed that at yielding condition, the steel bars, concealed steel plates, and strengthened steel plates at the bottom tensile region all yield. The maximum stress of steel bars is 417.5 MPa which is close to the measured yielding stress and the maximum stress of steel plates of 300 MPa. The stress of the steel bars and steel plates at the bottom is larger than in other regions. The maximum stress of the concealed steel plates appears at the interface of the concealed and strengthened steel plates and the stress of the concealed steel plates at the bottom of column also is high. This agrees well with the experimental results.

The stress diagrams of steel bars, concealed steel plates and strengthened steel plates of SRCJ-3 at peak condition are shown in Fig. 14. It can be observed that at peak condition, a large portion of the steel bars, concealed steel plates, and strengthened steel plates at both compressive and tensile bottom region yield. The maximum stress of steel bars, concealed steel plates, and strengthened steel plates are 427.2 MPa, 306.7 MPa, and 300 MPa, respectively. The stress of the concealed steel plates at the interface of concealed and strengthened steel plates is lower than at other parts which shows that the strengthened steel plates have a high restraint function.

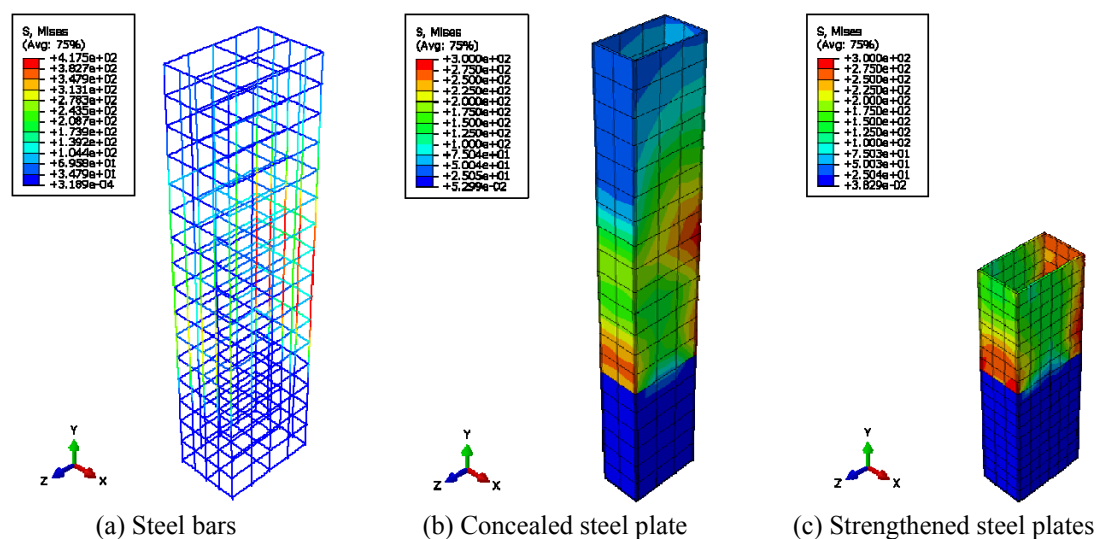


Fig. 13 Stress diagrams at yield condition

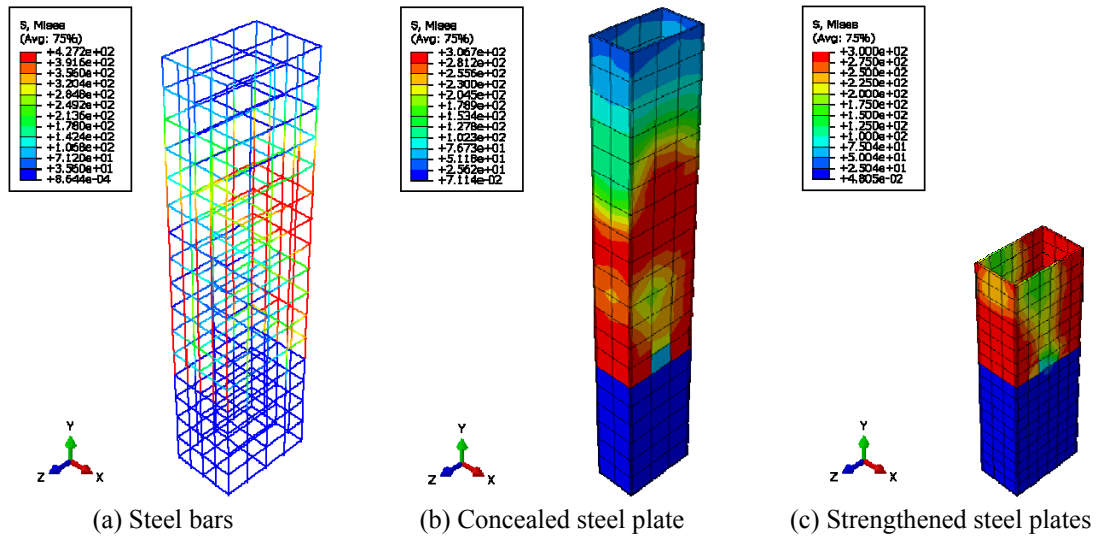


Fig. 14 Stress diagrams at peak condition

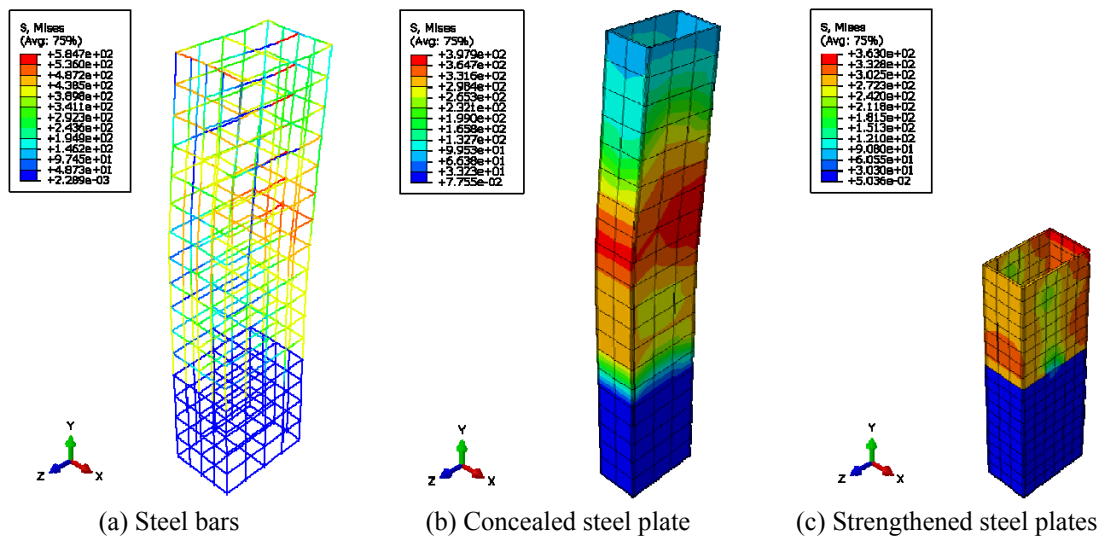


Fig. 15 Stress diagrams at damage condition

The stress diagrams of steel bars, concealed steel plates, and strengthened steel plates of SRCJ-3 at damage condition are shown in Fig. 15. It can be observed that at damage condition, all the steel bars and steel plates at the bottom compressive and tensile region yield. The stress of steel bars, concealed steel plates, and strengthened steel plates are 584.7 MPa, 397.9 MPa, and 363.0 MPa, respectively. The maximum stress of the strengthened steel plates appears at the interface of the concealed and strengthened steel plates. This shows that the strengthened steel plates have a high restraint function and agree well with the experimental results.

5.2.2.2 CFSG-3

The stress diagrams of steel tubes and strengthened steel plates of CFSJ-3 at yielding condition are shown in Fig. 16. All stresses are expressed in MPa. It can be observed that at yielding condition, the maximum stress of steel tubes is 372.1 MPa and the maximum stress of strengthened steel plates is 347.8 MPa. The latter and the former are close to each other which shows that the deformation of them are in agreement. The maximum stress of steel tubes appears at the interface of the strengthened and inner steel plates. The maximum stress of strengthened steel plates appears at the bottom of compressive zone and the stress of the four corner of the strengthened steel plates also is high.

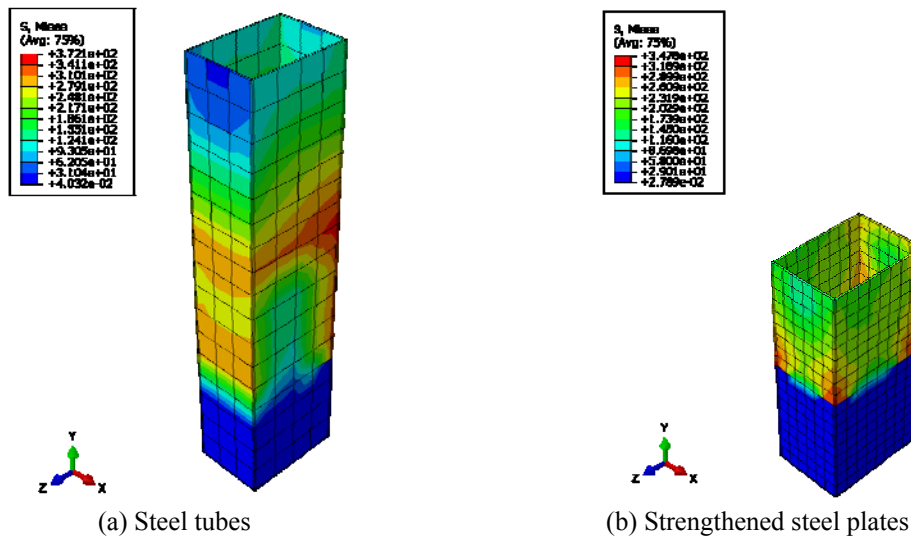


Fig. 16 Stress diagrams at yielding condition

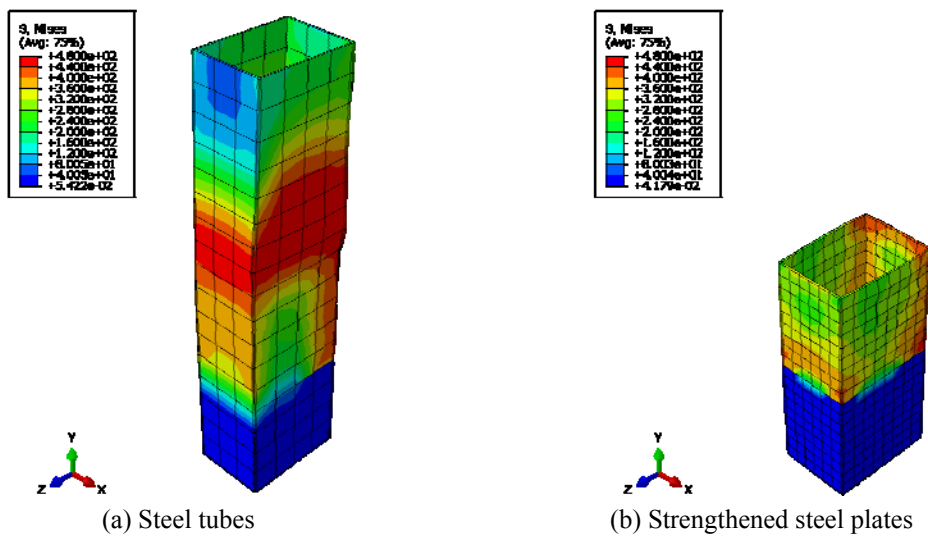


Fig. 17 Stress diagrams at peak condition

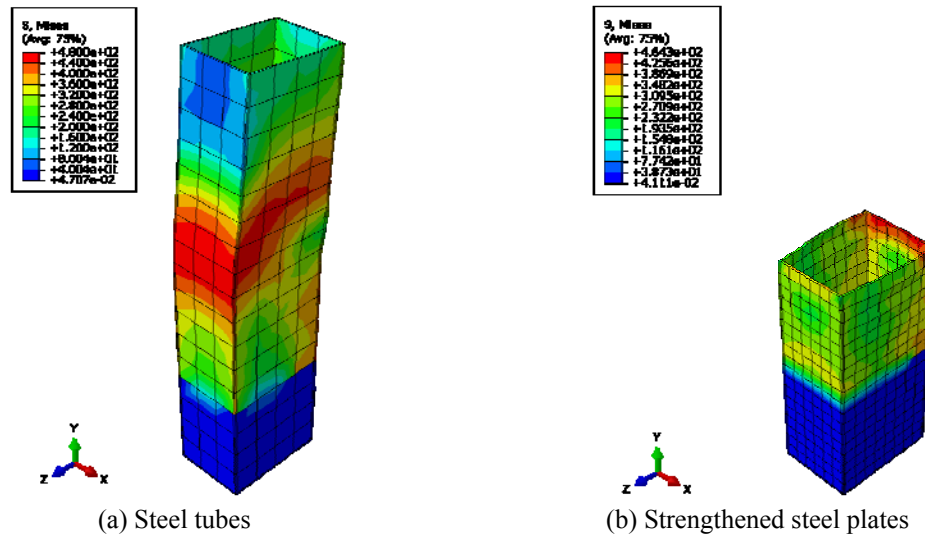


Fig. 18 Stress diagrams at peak condition

The stress diagrams of steel tubes and strengthened steel plates at peak condition of CFSJ-3 are shown in Fig. 17. It can be observed that at peak condition and because of the restraint function of the strengthened steel plates, the stress of the steel tube at the bottom zone is less than at the upper zone of the interface between the steel tube and the strengthened steel plates.

The stress diagrams of steel tubes and strengthened steel plates at damage condition of CFSJ-3 are shown in Fig. 18. It can be observed that at damage condition, the maximum stress of the inner rectangular steel tubes appears at the interface of the strengthened and inter steel plates while the maximum stress of strengthened steel plates appears at the interface of the compressive zone. Because of the restraint effect of the strengthened steel plates, the stress of inner steel tube is not large.

6. Conclusions

- Comparing with the conventional rectangular SRC and CFST composite columns, the strengthened rectangular SRC and CFST composite columns with strengthened steel plates have higher load-bearing capacity and better comprehensive seismic energy dissipation capacity. They can well realize the anti-earthquake ductility design purpose of the strong shear weak bending.
- Because of the restraint effect of the strengthened steel plates, the sectional flexural bearing capacity of the bottom strengthened region of the bottom strengthened rectangular CFST columns improves notoriously, meanwhile the shear-bearing capacity also improves significantly. It not only realizes the design purpose of the strong shear weak bending, but also develops the energy dissipation of bending deformation and shear deformation fully and matches each other. They exhibit high comprehensive seismic energy dissipation capacity.
- The load-displacement curves of the SRC and CFST composite columns from the elastic-plastic finite element analysis are in good agreement with the measured skeleton curves.

The load-bearing capacity of the finite element analysis fits well with the experimental results. Therefore, the finite element model can be used to simulate the loading states of composite columns.

- The proposed load-bearing capacity mechanic models and calculation formulas for rectangular SRC and CFST composite columns are based on experimental results. The calculated results are in good agreement with the experimental results. Therefore, these models can be used to calculate the load-bearing capacity and design of composite columns.
- The proposed of rectangular SRC and CFST composite columns exhibit high seismic energy dissipation capacity and can be used in the practical engineering.

Acknowledgments

This paper was supported by the National Natural Science Foundation of China under Grant No. 51178010, the Science and Technology Key Project of Beijing under Grant No. 8131002 and the Scientific and Technological Planning of Beijing Key Project Education Commission under Grant No. KZ200910005008.

References

- Cai, J. and Long, Y.L. (2007), "Axial load behavior of rectangular CFT stub columns with binding bars", *Adv. Struct. Eng.*, **10**(5), 551-565.
- Cao, W.L., Hui, C., Dong, H.Y., Xu, F.F. and Qiao, Q.Y. (2013), "Study on seismic behavior of bottom strengthened rectangular steel tube reinforced concrete columns", *World Earthq. Eng.*, **29**(3), 14-21.
- CECS 159:2004 (2004), Technical Specification for Structures with Concrete-filled Rectangular Steel Tube Members, China Planning Press, Beijing, China.
- Chen, Y.Y., Wang, H.S., Zhao, X.Z., Hu, J.L., Wang, D.S., Jiang, W.W. and Bao, L.J. (2008), "Experimental study on hysteretic behavior of SRC columns with high ratio of core steel", *J. Build. Struct.*, **29**(3), 31-39.
- Choi, Y.H., Kim, K.S. and Choi, S.M. (2008), "Simplified P-M interaction curve for square steel tube filled with high-strength concrete", *Thin-Wall. Struct.*, **46**(5), 506-515.
- Chung, K., Chung, J. and Choi, S. (2007), "Prediction of pre- and post-peak behavior of concrete-filled square steel tube columns under cyclic loads using fiber element method", *Thin-Wall. Struct.*, **45**(9), 747-758.
- Elwan, S.K. and Rashed, A.S. (2011) "Experimental behavior of eccentrically loaded R.C. short columns strengthened using GFRP wrapping", *Struct. Eng. Mech., Int. J.*, **39**(2), 207-221.
- Elwan, S.K. and Omar, M.A. (2014) "Experimental behavior of eccentrically loaded RC slender columns strengthened using GFRP wrapping", *Steel Compos. Struct., Int. J.*, **17**(3), 271-285.
- GB 50010-2010 (2010), Code for Design of Concrete Structure, China Architecture and Building Press, Beijing, China.
- Han, L.H., Ren, Q.X. and Li, W. (2010), "Tests on inclined, tapered and STS concrete-filled steel tubular (CFST) stub columns", *J. Constr. Steel Res.*, **66**(10), 1186-1195.
- Hui, C., Cao, W.L., Dong, H.Y. and Xu, F.F. (2012), "Study on seismic behavior of bottom strengthened rectangular concrete filled steel tube columns", *World Earthq. Eng.*, **28**(4), 161-169.
- JGJ 138-2001 (2001), Technical Specification for Steel Reinforced Concrete Composite Structure, China Architecture and Building Press, Beijing, China.
- Liao, F.Y. and Han, L.H. (2010), "Performance of concrete-filled steel tube reinforced concrete columns with square sections", *Eng. Mech.*, **27**(4), 153-162.

- Lu, X.L., Yin, X.W. and Jiang, H.J. (2014), "Experimental study on hysteretic properties of SRC columns with high steel ratio", *Steel Compos. Struct., Int. J.*, **17**(3), 287-303.
- Sav, V., Campian, C. and Senila, M. (2011), "Composite steel-concrete columns with high strength concrete versus normal strength concrete", *Civil Eng. Arch.*, **54**(1), 74-81.
- Weng, C.C., Yin, Y.L., Wang, J.C. and Liang, C.Y. (2008), "Seismic cyclic loading test of SRC columns confined with 5-spirals", *Sci. China Ser. E-Tech. Sci.*, **51**(5), 529-555.
- Yu, Z.W., Ding, F.X. and Cai, C.S. (2007), "Experimental behavior of circular concrete-filled steel tube stub columns", *J. Constr. Steel Res.*, **63**(2), 165-174.
- Zhou, X.H., Liu, J.P. and Zhang, S.M. (2010), "Seismic behavior of ultra short columns of square tubed high strength reinforced concrete", *China Civil Eng. J.*, **43**(8), 1-10.

CC